

Article

# A Tailor-Made Protocol to Synthesize Yolk-Shell Graphene-Based Magnetic Nanoparticles for Nanomedicine

Raquel O. Rodrigues <sup>1,2</sup>, Giovanni Baldi <sup>3</sup>, Saer Doumett <sup>3</sup>, Juan Gallo <sup>4</sup>,  
Manuel Bañobre-López <sup>4</sup>, Goran Dražić <sup>5</sup>, Ricardo C. Calhella <sup>1</sup>, Isabel C. F. R. Ferreira <sup>1</sup>,  
Rui Lima <sup>6,7</sup>, Adrián M. T. Silva <sup>2</sup> and Helder T. Gomes <sup>1,2,\*</sup>

<sup>1</sup> Centro de Investigação de Montanha (CIMO), Instituto Politécnico de Bragança, 5300-253 Bragança, Portugal; raquel.rodrigues@ipb.pt (R.O.R.); calhella@ipb.pt (R.C.C.); iferreira@ipb.pt (I.C.F.R.F.)

<sup>2</sup> Laboratory of Separation and Reaction Engineering—Laboratory of Catalysis and Materials (LSRE-LCM), Faculdade de Engenharia, Universidade do Porto, Rua Dr. Roberto Frias, 4200-465 Porto, Portugal; adrian@fe.up.pt

<sup>3</sup> CERICOL—Centro Ricerche Colorobbia, Via Pietramarina 123, 50053 Sovigliana—Vinci, Firenze, Italy; baldig@colorobbia.it (G.B.); DOUMETTS@colorobbia.it (S.D.)

<sup>4</sup> Advanced (magnetic) Theranostic Nanostructures Lab, Life Sciences Department, INL—International Iberian Nanotechnology Laboratory, Av. Mestre José Veiga, 4715-330 Braga, Portugal; juan.gallo@inl.int (J.G.); manuel.banobre@inl.int (M.B.-L.)

<sup>5</sup> Department for Materials Chemistry, National Institute of Chemistry, Hajdrihova 19, SI-1001 Ljubljana, Slovenia; goran.drazic@gmail.com

<sup>6</sup> METRICS—Centro de Engenharia Mecânica e Sustentabilidade de Recursos, Mechanical Engineering Department, University of Minho, Campus de Azurém, 4800-058 Guimarães, Portugal; rl@dem.uminho.pt

<sup>7</sup> CEFT—Centro de Estudos de Fenómenos de Transporte, Faculdade de Engenharia, Universidade do Porto, Rua Dr. Roberto Frias, 4200-465 Porto, Portugal

\* Correspondence: htgomes@ipb.pt; Tel.: +351 273303110

Received: 18 September 2018; Accepted: 9 October 2018; Published: 13 October 2018



**Abstract:** A simple tailor-made protocol to synthesize graphene-based magnetic nanoparticles (GbMNPs) for nanomedicine is herein reported. Different GbMNPs with very distinctive physicochemical and toxicological properties were synthesized by adjusting the number of carbon precursors in the coating of superparamagnetic iron oxide nanoparticles. In vitro tests show the ability to use these GbMNPs as intelligent and on-demand drug nanocarrier systems for drug delivery, exhibiting the following features: good colloidal stability, good loading capacity of the chemotherapeutic drug doxorubicin, high pH-controlled release of the encapsulated drug (targeting tumour acidic pH conditions), superparamagnetic behaviour and biocompatibility. Due to their combined properties (i.e., physicochemical, magnetic, and biocompatibility), GbMNPs show high potentiality to be combined with other biomedical techniques, such as magnetic hyperthermia, which can represent an enhancement in the treatment of cancer.

**Keywords:** graphene magnetic nanocomposites; drug delivery; DOX cancer

## 1. Introduction

In order to overcome magnetic nanoparticle limitations, such as toxicity, self-aggregation and a low rate of bio-functionalization, many composite magnetic nanosystems have been developed in the last decade for nanomedicine [1,2]. These nanostructures are usually developed by having a magnetic core covered with a metal or a non-metal structure, such as gold [3–5], silica [6,7], polymers [8–10], among others. In general, this core-shell approach allows for, besides protection of the magnetic core,

the anchoring of various therapeutic drugs or biomolecules for targeted drug delivery, improved biocompatibility, and prolonged blood circulation half-life [11,12]. Nevertheless, when developed for drug delivery applications, these systems generally show some limitations, such as a low drug loading capacity and poor or absence of stimuli-responsive controlled release. Thus, additional efforts are necessary to add capping scaffolds on the surface of these nanoparticles (e.g., polymers, inorganic nanoparticles, and biomacromolecules), acting as gatekeepers to enable a controlled drug release in response to endogenous (i.e., pH, enzymes, among others) or exogenous (i.e., light, temperature changes, among others) stimuli [13,14]. However, the laborious synthetic protocols proposed to date hinder the technology transfer to industry. Although the apparent success of nanoparticles developed and tested at laboratory scale is high, the translation of nanomedicine products to clinical applications has been limited and slow [15]. In fact, it is estimated that less than 200 nanomedicine products have been commercialized so far [16]. This phenomenon has been attributed by two main factors: (1) the inability of current biological models to predict the nanoparticles-cells/organs bio-interactions [16], and (2) the complex synthetic procedures that just produce a small number of nanomedicine products [17].

Carbon-based magnetic nanoparticles provide high chemical and thermal stability, a large surface area, biocompatibility and simple functionalization [14,18]. Recent studies, such as those published by Huang et al., 2016 [13] and Sasikale et al., 2016 [19], have shown that graphene-based materials, including graphene derivatives such as graphene oxide (GO), can be used as pH-responsive controlled release systems. This promising capability of graphene-based materials is attributed to  $\pi$ - $\pi$  stacking interactions allowing the adsorption of a variety of aromatic biomolecules, as well as to the presence of oxygen and hydrogen-containing surface groups promoting hydrogen bond interactions. However, the synthesis of magnetic nanoparticles combined with graphene derivatives generally demands toxic chemicals (e.g., those employed in the Hummers' method to produce GO [20]), or complex techniques/methods (e.g., in chemical vapour deposition [21]), often limited to the production of nanoparticles in a very small scale.

In order to suppress these limitations, a simple procedure to produce graphene-based magnetic nanoparticles (GbMNPs) is herein presented, which provides different types of GbMNPs by adjusting the concentration of the carbon precursors. The reported tailor-made protocol allows us to synthesize smart drug nanocarrier systems for cancer treatment, revealing (i) a high loading of the chemotherapeutic drug doxorubicin; (ii) a strong pH stimuli-responsive controlled release; (iii) a high Saturation magnetization ( $M_s$ ) profile; and (iv) a good biocompatibility.

## 2. Materials and Methods

### 2.1. Chemicals

Iron(III) chloride hexahydrate,  $\text{FeCl}_3 \cdot 6\text{H}_2\text{O}$  (97%), and formaldehyde (37 wt % stabilized with methanol) were supplied by Panreac. The ammonium hydroxide solution,  $\text{NH}_4\text{OH}$  (25 wt % in  $\text{H}_2\text{O}$ ), was acquired from Merck. Iron (II) chloride tetrahydrate,  $\text{FeCl}_2 \cdot 4\text{H}_2\text{O}$  (99 wt %), ethanol absolute,  $\text{C}_2\text{H}_6\text{O}$  (99.8%), nitric acid,  $\text{HNO}_3$  (70 wt %), sodium phosphate monobasic,  $\text{NaH}_2\text{PO}_4$  (99.0 wt %), sodium phosphate dibasic,  $\text{Na}_2\text{HPO}_4$  (99.0 wt %), sodium chloride,  $\text{NaCl}$  (99.5 wt %), potassium chloride,  $\text{KCl}$  (99 wt %), and sodium hydroxide,  $\text{NaOH}$  (98 wt %), were purchased from Sigma-Aldrich (St. Louis, MO, USA). Resorcinol (98 wt %) was obtained from Fisher chemicals (Hampton, NH, USA). Tetraethyl orthosilicate (TEOS) (98 wt %), was supplied from Fluka (St. Louis, MO, USA). Doxorubicin hydrochloride (DOX) (98 wt %), was purchased from Discovery Fine Chemicals (Wimborne, UK).

The breast cell line MCF-7 (Michigan Cancer Foundation-7) was acquired from Deutsche Sammlung von Mikroorganismen and Zellkulturen GmbH (DSMZ, Braunschweig, Germany). Roswell Park Memorial Institute (RPMI) 1640 medium, Hank's balanced salt solution (HBSS), fetal bovine serum (FBS), L-glutamine, trypsin-ethylenediaminetetraacetic acid (trypsin-EDTA),

penicillin/streptomycin solution ( $100 \text{ U}\cdot\text{mL}^{-1}$  and  $100 \text{ mg}\cdot\text{mL}^{-1}$ , respectively) were purchased from Gibco Invitrogen Life Technologies (Carlsbad, CA, USA).

## 2.2. Synthesis of GbMNPs

The synthesis procedure of GbMNPs was divided into two stages, i.e., the synthesis of the magnetic core followed by the graphene-based shell formation, as illustrated in Figure 1.

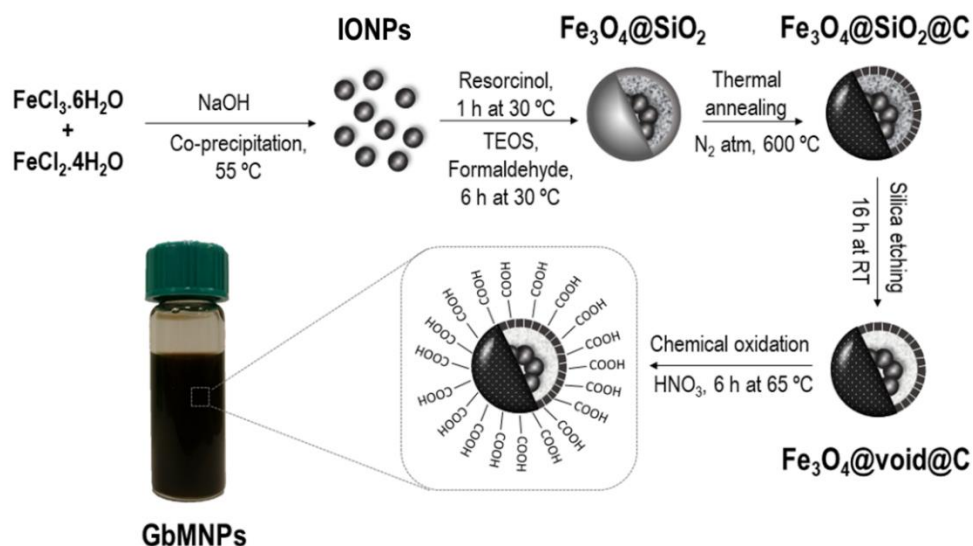


**Figure 1.** The schematic representation of the synthetic steps involved in the development of the graphene-based yolk-shell magnetic nanoparticles (GbMNPs).

The synthesis of the iron oxide core, with a mean diameter of 18 nm, was achieved through co-precipitation of  $\text{Fe}^{2+}$  and  $\text{Fe}^{3+}$  (with a molar ratio of 1:2) in a basic solution of ammonium hydroxide at  $55^\circ\text{C}$ , following the procedure described elsewhere [22,23].

Subsequently, the graphene-based shell was accomplished via a one-pot strategy of hydrolysis and polymerisation of the precursors, i.e., resorcinol, formaldehyde, and TEOS [23,24]. Different GbMNPs, with different hollow cavities between the shell and the magnetic core, were obtained using different amounts of these precursors in relation to a fixed mass of the magnetic core, adapting the procedure described elsewhere (c.f. Table 1) [24]. In brief, a solution containing 0.25 g of iron oxide with 150 mL of ethanol and 50 mL of deionized water was sonicated and transferred into a 250 mL two-necked round-bottom flask. Then, resorcinol and ammonium hydroxide were added to the solution and continuously stirred for 1 h at  $30^\circ\text{C}$ . Then, the formaldehyde, and TEOS solutions were added and stirred at  $30^\circ\text{C}$  for 6 h. The solution was then heated at  $80^\circ\text{C}$  under constant stirring for another 8 h. The magnetic product resulting from this protocol was washed using deionized water and absolute ethanol. The resulted magnetic nanostructures were annealed under a  $\text{N}_2$  flow ( $100 \text{ cm}^3\cdot\text{min}^{-1}$ ) in a tubular vertical oven at  $120^\circ\text{C}$  and  $400^\circ\text{C}$  during 60 min at each temperature, and then at  $600^\circ\text{C}$  for 240 min, defining a heating ramp of  $2^\circ\text{C}\cdot\text{min}^{-1}$ . In the last step, the silica was removed by etching in a strongly basic  $\text{NaOH}$  solution ( $10 \text{ mol}\cdot\text{L}^{-1}$ , 16 h at room temperature with stirring), resulting in the graphene-based magnetic nanoparticles (GbMNPs) with a yolk-shell nanostructure.

**Table 1.** The effect of the amount of the precursor resorcinol, formaldehyde, and tetraethyl orthosilicate (TEOS), over the shell and void thicknesses of GbMNPs.

Material	Magnetic Core (g)	Resorcinol (g)	Formaldehyde (mL)	TEOS (mL)	Hollow Thickness (nm) <sup>a</sup>	Carbon-Shell Thickness (nm) <sup>a</sup>
GbMNP-1	0.25	0.05	0.075	0.10	Not detected	1.41 ± 0.44
GbMNP-2	0.25	0.10	0.150	0.21	0.70 ± 0.30	3.55 ± 1.27
GbMNP-3	0.25	0.20	0.300	0.41	2.07 ± 0.92	7.07 ± 1.88

<sup>a</sup> Determined by using ImageJ software from HR-STEM images as mean ± standard deviation ( $n = 60$ ).

### 2.3. Colloidal Stabilization of GbMNPs

To ensure the hydrophilization of the GbMNPs in aqueous solutions, the graphene-based shells were chemically functionalized by an acid treatment at mild conditions. In brief, the functionalization run was conducted in a 250 mL round-bottom flask at 65 °C under vigorous magnetic stirring (C-Mag HS7, IKA, Staufen, Germany). The samples of GbMNPs (5 mg·mL<sup>-1</sup>) were oxidized with HNO<sub>3</sub> (1 mol·L<sup>-1</sup>) during 6 h. The activated GbMNPs were washed several times in deionized water and absolute ethanol. The resulting material was dried overnight at 60 °C. The obtained hydrophilic GbMNPs were used to perform the drug delivery studies with doxorubicin (DOX).

### 2.4. Characterization of GbMNPs

A wide-angle powder X-ray diffraction (XRD) analysis was carried out in an Expert Pro Philips X-Ray diffractometer (Malvern Panalytical's, Egham, UK) using a Cu K $\alpha$  radiation ( $\lambda = 1.54 \text{ \AA}$ ).

The Raman spectra of the samples were recorded using a micro-Raman spectrometer apparatus (Micro-Raman DXR, Thermo Scientific, Waltham, MA, USA) with a 532 nm laser excitation.

A High-Resolution Transmission Electron Microscope (HR-TEM) using a Cs-corrected probe (ARM 200 CF, Joel, Akishima, Japan) was used to obtain the morphology and microstructure of the GbMNPs.

The amounts of carbon and magnetic core in the as-synthesized GbMNPs were determined by thermogravimetric (TG) analysis (STA 449 C Jupiter, Netzsch, Goa, India) and the samples were heated in air flow from 50 °C to 950 °C, at 20 °C·min<sup>-1</sup>.

The textural properties of GbMNPs were obtained using N<sub>2</sub> adsorption-desorption isotherms at -196 °C (Quantachrome NOVA 4200e, Boynton Beach, FL, USA), as reported elsewhere [23].

The pH at the point of zero charge (pH<sub>PZC</sub>) of the materials was determined by adapting the methodology described elsewhere [25].

The magnetic properties of the superparamagnetic core and GbMNPs were explored with a superconducting quantum interference device (SQUID-VSM) magnetometer (Quantum Design, San Diego, CA, USA). Hysteresis curves were recorded for magnetic fields between -20 kOe and 20 kOe at 27 °C.

### 2.5. Drug Loading Studies

The drug loading studies were performed by mixing a given amount of DOX (10 to 300  $\mu\text{g}\cdot\text{mL}^{-1}$ ) and a fixed amount of GbMNPs (500  $\mu\text{g}\cdot\text{mL}^{-1}$ ) in a shaking incubator (VWR, Radnor, PA, USA) during 24 h, in the dark, at room temperature. The resulting GbMNPs encapsulated with the drug (GbMNPs-DOX) were collected by centrifugation at 15,000 rpm for 30 min, and the supernatant used to determine the DOX concentration by Ultraviolet-visible spectroscopy (UV-Vis, Bruker, Billerica, MA, USA) at 480 nm. The drug loading efficiency and drug loading capacity were calculated using Equations (1) and (2), respectively.

$$\text{Drug loading efficiency (\%)} = \frac{\text{Initial concentration of drug} - \text{Drug content in the supernatant}}{\text{Initial concentration of drug}} \times 100 \quad (1)$$

$$\text{Drug loading capacity } (\mu\text{g}\cdot\text{mg}^{-1}) = \frac{\text{mass of drug loaded}}{\text{mass of GbMNPs}} \quad (2)$$

### 2.6. In Vitro pH-Dependent Drug Release and Kinetics Studies

The in vitro pH-dependent drug release of DOX from GbMNPs was performed by using freeze-dried GbMNPs-DOX samples (2.0 mg) suspended in a phosphate buffer solution (20 mL) at physiological and acidic pHs (7.4, 6.0 and 4.5) using a shaking incubator at 37 °C. The pH-dependent release of DOX was determined along selected time intervals (0.5, 1, 2, 3, 4, 6, 8, 24, and 48 h), by collecting samples from the different suspensions of GbMNPs-DOX in phosphate buffers solutions (pH 4.5, 6.0, and 7.4). The samples were centrifuged, and the supernatant used to monitor the released DOX at 480 nm in UV-Vis. The drug release kinetics was studied by fitting the drug release data with zero-order (release independent of concentration), first-order (release dependent of concentration), Hixson-Crowell (release by dissolution), Higuchi (release by diffusion), and Korsmeyer-Peppas (log (cumulative drug release) versus log (time) models, by comparing the regression coefficient ( $R^2$ ) values obtained for the different models.

### 2.7. In Vitro Biostudies

The developed graphene-based magnetic nanocomposites were investigated to confirm their biocompatibility and cellular drug-delivery performance.

#### 2.7.1. Cell Culture

The biocompatibility and cellular drug-delivery assays were assessed by using two cell lines, namely porcine liver primary cells (PLP2) [26], and a human breast tumour cell line (MCF-7). Cell lines were cultured and maintained prior to the in vitro studies in RPMI-1640 medium containing 10% foetal bovine serum (FBS), 1% of glutaraldehyde, 1% of penicillin, and 1% of streptomycin, under a humid atmosphere containing 5% of CO<sub>2</sub>, at 37 °C.

#### 2.7.2. Biocompatibility and Cellular Drug-Delivery Assay

In vitro biocompatibility and cellular drug-delivery studies were assessed by using sulforhodamine B (SRB) colourimetric assay, as described elsewhere [27]. Briefly, the cell lines were seeded in 96-well plates, at an initial cell density of  $1.0 \times 10^4$  cells/well. The biocompatibility of the GbMNPs was assessed with the primary cell culture, PLP2, using different concentrations of the free-drug nanocarriers (0.12 to 30.0  $\mu\text{g}\cdot\text{mL}^{-1}$ ). For the in vitro cellular drug-delivery effect, the tumour cell line, MCF-7, and primary cell culture, PLP2, were tested and treated with a series of free DOX and GbMNPs-DOX containing the same amount of free DOX in the tests (0.03, 0.12, 0.47, 1.88, and 7.50  $\mu\text{g}_{(\text{DOX})}\cdot\text{mL}^{-1}$ ). As blanks, the control wells just containing cells with the cultured medium were used. For statistical analysis, two individual tissue-culture plates were used, and all the assays performed in duplicate wells ( $n = 4$ ). The statistical analysis was performed with the Student's *t*-test with a significance level of  $p < 0.05$ , shown as asterisks (\*), using Microsoft Office Excel (version Professional Plus 2013).

## 3. Results and Discussion

### 3.1. Synthesis and Characterization of the GbMNPs

The synthesis of the magnetic core and graphene-based shell formation is represented in Figure 1. HR-TEM micrographs (Figure 2) confirmed the formation of the yolk-shell magnetic nanoparticles, i.e., the iron oxide cores shelled by a graphene-based layer. As expected, the increment of the amount of carbon-based precursors (resorcinol, formaldehyde and TEOS) in relation to a fixed mass of the magnetic core provided an increase of the void and graphene-based shell thickness, as determined

using the ImageJ software (1.46r, NIH, Bethesda, MD, USA) (Table 1). Thus, three different types of GbMNPs were synthesized with different hollow cavities and graphene-based shell thicknesses.

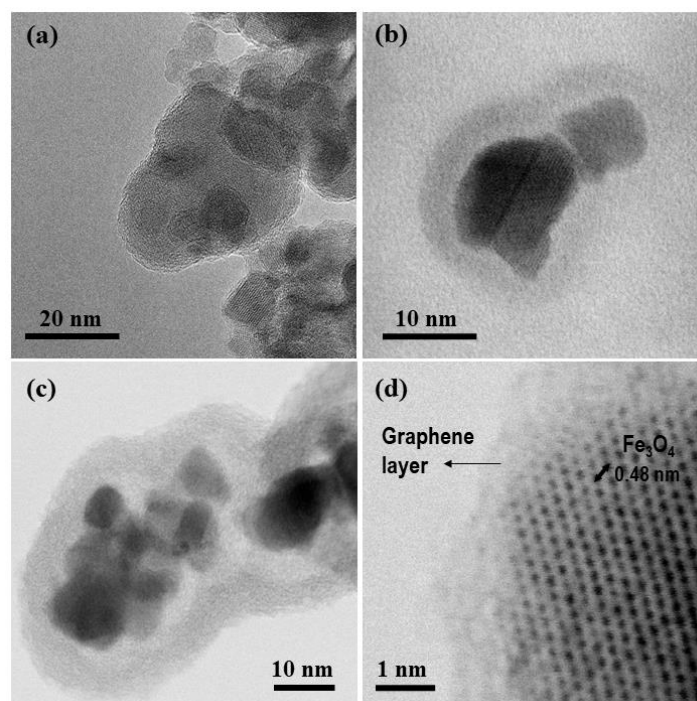


**Figure 2.** The high-resolution transmission electron microscopy (HR-TEM) bright field images of samples: (a) GbMNP-1; (b) GbMNP-2; (c) GbMNP-3; and (d) the detail of the magnetic core of iron oxide covered by a few graphene layers in sample GbMNP-2.

Interestingly, the graphene-based shell thickness increased in the same proportion as the amount of the precursors used. Thus, by doubling the number of carbon precursors from GbMNP-1 to GbMNP-2 and GbMNP-3, the shell thickness was successively doubled, as listed in Table 1. HR-TEM images also allowed for the determination of a lattice spacing of 0.48 nm, indicating that the magnetic core consisted of iron oxide nanoparticles, as further confirmed by XRD analysis (Figure 3a).

Figure 3a shows the XRD patterns for GbMNPs and the iron oxide material used as the magnetic core. The  $2\theta$  peaks (111), (220), (311), (222), (400), (422), (511), and (440), are ascribed as the characteristic diffraction peaks of  $\text{Fe}_3\text{O}_4$  nanoparticles (JCPDS no. 19-629). Some other peaks were observed for GbMNP-2 corresponding to (110) and (211) and assigned as metal iron, probably caused by the reduction of the magnetic core through the thermal annealing procedure (600 °C) in an inert atmosphere [23]. In addition, the presence of the graphene-based material is ascribed by the presence of a peak at  $24.3^\circ$  (002) [28].

Results from the TG analysis are shown in Figure 3b. The first significant weight loss below 150 °C can be ascribed to the removal of water molecules physisorbed on the surface of GbMNPs. The sharp mass loss observed between 450–600 °C is attributed to the combustion of the carbon material [29–33], revealing mass percentages of the carbon-based shells in the samples of 0.5%, 9.7%, and 18.2% for GbMNP-1, GbMNP-2, and GbMNP-3, respectively. In addition, the mass of the magnetic core was calculated as 97.7%, 88.0%, and 77.8% for GbMNP-1, GbMNP-2, and GbMNP-3, respectively.

The Raman spectra of GbMNP-2 and GbMNP-3 are shown in Figure 3c,d, respectively. Graphene oxide (GO) is suggested in these samples by the D peak at  $1350\text{ cm}^{-1}$ , the conventional G peak at  $1582\text{ cm}^{-1}$  and the 2D peak at  $2816\text{ cm}^{-1}$  [34]. On the other hand, the Raman spectrum of the sample GbMNP-1 did not show any of these peaks (data not shown), most probably due to the very low amount of graphene-based shell in this sample (0.5%, determined by TG analysis). Thus, the GbMNP-1 sample was not considered in the following studies.

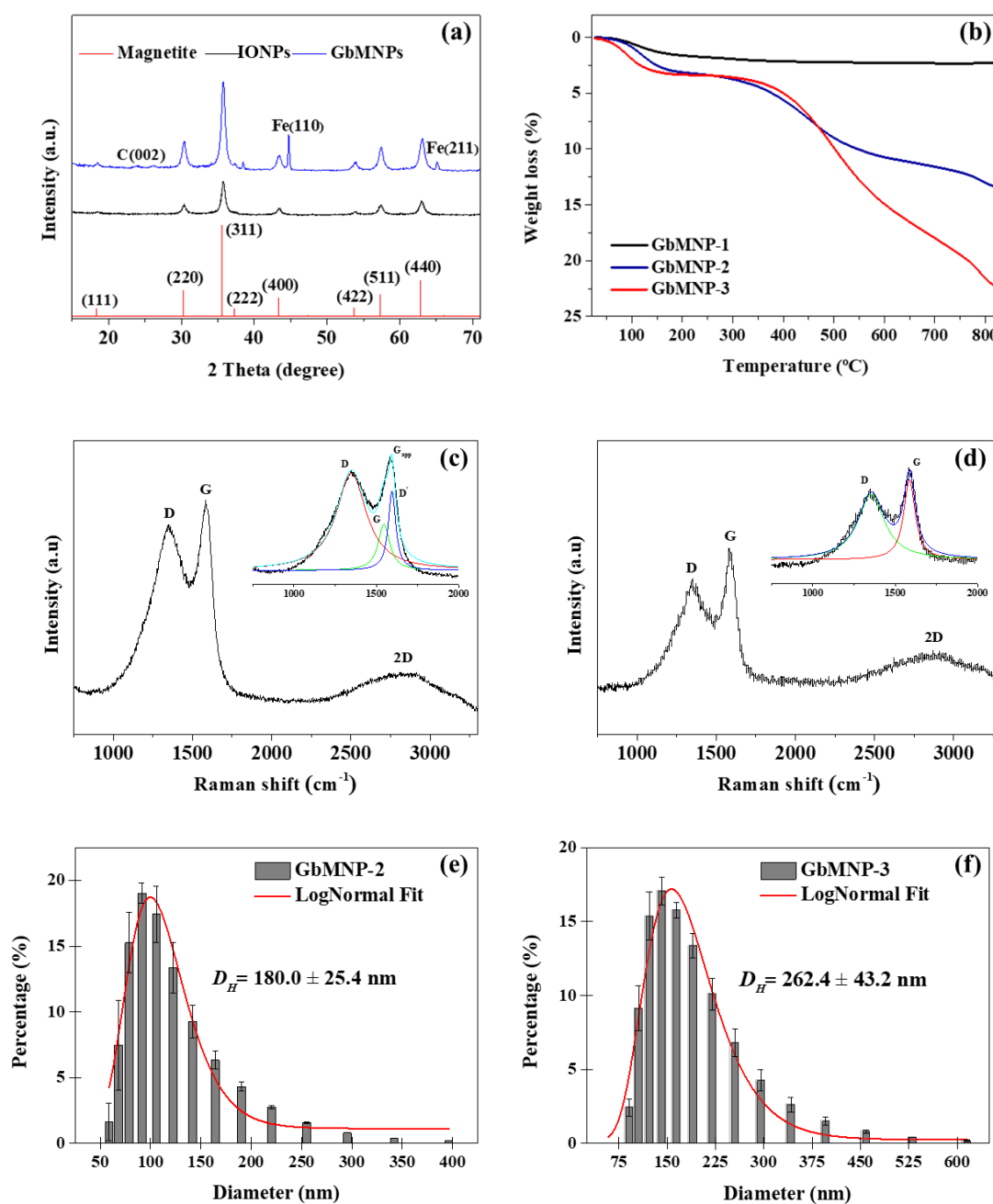


**Figure 3.** The physicochemical characterization of GbMNPs: (a) Wide-angle powder X-ray diffraction (XRD) patterns of iron oxide nanoparticles and GbMNP-2; (b) Thermogravimetric analysis of the as-synthesized GbMNPs (GbMNP-1, GbMNP-2, and GbMNP-3); Raman spectrum of the as-synthesized GbMNPs with an inset corresponding to the deconvolution of the observed D and G (c) GbMNP-2; (d) GbMNP-3; Dynamic light scattering (DLS) measurements with average hydrodynamic diameter ( $D_H$ ) of (e) GbMNP-2; (f) GbMNP-3.

The integrated peak intensity between  $I_D$  and  $I_G$  was found as 1.61 for sample GbMNP-2 (using the new deconvoluted G peak), corresponding to a disordered GO structure [34,35], and 0.43 for the sample GbMNP-3 (using the conventional G peak, since no deconvoluted peak was found), indicating the presence of a defective multi-graphitic-layer shell [36], which was also observed by HR-TEM (Figure 2c). Furthermore, the deconvolution of the conventional G band—in this case, the apparent G band ( $G_{app}$ ), brings in evidence the actual G ( $1546\text{ cm}^{-1}$ ) and the D' ( $1594\text{ cm}^{-1}$ ) bands, which can be assigned for sample GbMNP-2, but not clearly for sample GbMNP-3. Interestingly, the D' band was

reported by Kaniyoor and Ramaprabhu [37] as evidence of the presence of a few layers of wrinkled graphene-based (FlwG) structures, which is in line with the observed shell nanostructure found in GbMNP-2 (cf. Figure 2d).

Dynamic light scattering (DLS) measurements (Figure 3d,e) show that the average hydrodynamic diameter of the samples increased with the increment of the carbon precursors.

The main textural properties of the synthesized GbMNPs are given in Table 2. Specific surface areas ( $S_{\text{BET}}$ ) of 156 and 245  $\text{m}^2 \cdot \text{g}^{-1}$  were determined for the GbMNP-2 and GbMNP-3 materials, respectively. These relatively high surface areas, in comparison with that of bare magnetic nanoparticles ( $56 \text{ m}^2 \cdot \text{g}^{-1}$ ), are attributed to the graphene-based shell in the GbMNPs structure, the  $S_{\text{BET}}$  increasing with the shell thickness. The analysis of the  $V_{\text{micro}}/V_{\text{total}}$  ratios (0.041 and 0.105 for GbMNP-2 and GbMNP-3, respectively), reveals that the samples mainly contain mesopores. In addition, the average pore diameter of GbMNP-3 is lower than that of GbMNP-2 (5.4 and 8.2 nm, respectively). This phenomenon can be related to the increment of the thickness of the graphene-based shell between GbMNPs-2 and GbMNPs-3, which can lead to a denser and more microporous nanostructure. Overall, the GbMNPs samples, in comparison with uncoated magnetite, exhibit larger surface area and mesoporous nature, which are relevant characteristics for drug delivery applications, i.e., the encapsulation, transport, and release of biomolecules [23].

**Table 2.** The textural properties of the synthesized materials: specific surface area ( $S_{\text{BET}}$ ), non-microporous surface area ( $S_{\text{meso}}$ ), micropore volume ( $V_{\text{micro}}$ ), total pore volume ( $V_{\text{total}}$ ), ratio between micropore and total pore volume ( $V_{\text{micro}}/V_{\text{total}}$ ) and average pore diameter ( $d_{\text{average}}$ ).

Material	$S_{\text{BET}}$ ( $\text{m}^2 \cdot \text{g}^{-1}$ )	$S_{\text{meso}}$ ( $\text{m}^2 \cdot \text{g}^{-1}$ )	$V_{\text{micro}}$ ( $\text{cm}^3 \cdot \text{g}^{-1}$ )	$V_{\text{total}}$ ( $\text{cm}^3 \cdot \text{g}^{-1}$ )	$V_{\text{micro}}/V_{\text{total}}$	$d_{\text{average}}$ (nm)
GbMNP-2	156	123	0.013	0.318	0.041	8.2
GbMNP-3	245	160	0.035	0.333	0.105	5.4

The magnetic hysteresis curves acquired for iron oxide nanoparticles and GbMNPs are shown in Figure 4. The determined magnetic properties of these samples are listed in Table 3. Iron oxide nanoparticles (IONPs) exhibit a saturation magnetization ( $M_s$ ) of  $78 \text{ emu} \cdot \text{g}^{-1}_{\text{IONPs}}$ , but, as expected, the magnetic susceptibilities of the GbMNPs suffer a decrease with the increase of the graphene-based shell thickness to 69.8 and 61.2  $\text{emu} \cdot \text{g}^{-1}_{\text{IONPs}}$ , respectively for GbMNP-2 and GbMNP-3. The high  $M_s$  found on these GbMNPs can be attributed to the presence of small clusters of superparamagnetic magnetite, as suggested by the TEM images. Remarkably, the superparamagnetic-like behaviour of the GbMNPs was maintained, as shown by the low-field data (inset in Figure 4, and Table 3), where saturation remanence ( $M_r$ ) and low coercivity ( $H_c$ ) are negligible.

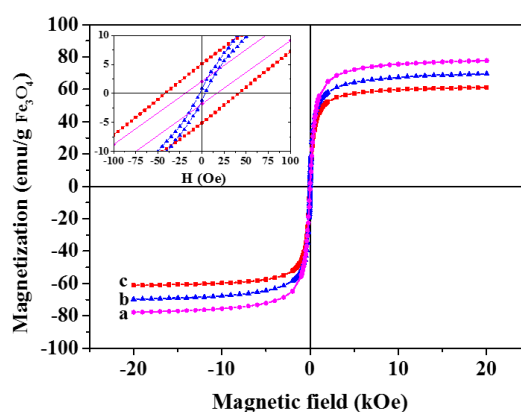


**Figure 4.** The magnetization curves of (a) IONPs; (b) GbMNP-2 and (c) GbMNP-3. Hysteresis loops at 27 °C up to  $\pm 20$  kOe; the inset corresponds to the zoom in the low field region.

**Table 3.** The magnetic properties of the uncoated IONPs and as-synthesized GbMNPs: saturation magnetization ( $M_s$ ), coercivity ( $H_c$ ), and saturation remanence ( $M_r$ ).

Sample	$M_s$ ( $\text{emu}\cdot\text{g}^{-1}$ IONPs)	$H_c$ (Oe)	$M_r$ ( $\text{emu}\cdot\text{g}^{-1}$ IONPs)
IONPs	77.7	18.33	1.94
GbMNP-2	69.8	3.54	1.16
GbMNP-3	61.2	41.33	5.08

### 3.2. DOX Loading Studies

Doxorubicin (DOX) is one of the chemotherapeutic drugs most commonly used [38], however, it presents several lethal side effects [39]. One of the strategies to overcome this toxicity issue is through targeted drug delivery. For this purpose, DOX was chosen to study the drug delivery properties of the developed GbMNPs. To assess the DOX loading and release, UV-Vis absorbance analysis at 480 nm was used [40]. The drug loading efficiency and drug loading capacity profiles were evaluated by ranging the initial DOX concentration between 10 to 300  $\mu\text{g}\cdot\text{mL}^{-1}$ , on a fixed amount of GbMNPs (500  $\mu\text{g}\cdot\text{mL}^{-1}$ ). The drug loading profiles are shown in Figure 5.

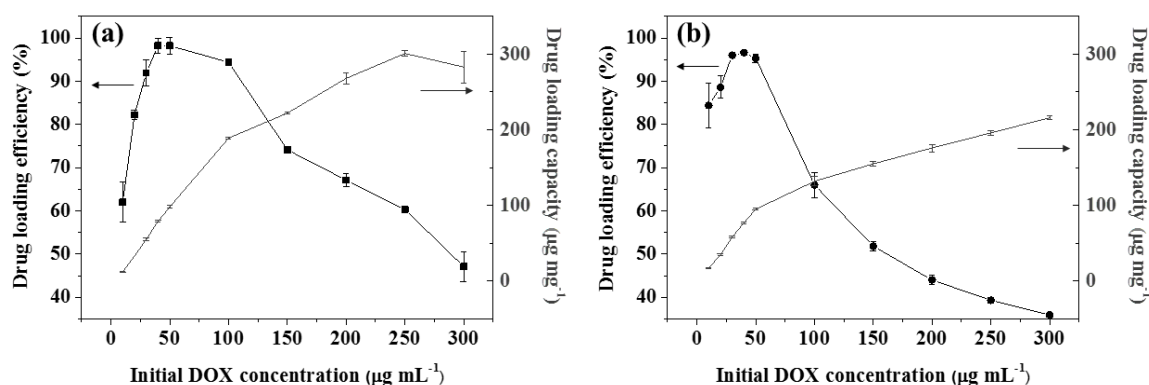


**Figure 5.** The drug loading profiles of GbMNPs at different initial doxorubicin (DOX) concentrations (10–300  $\mu\text{g}\cdot\text{mL}^{-1}$ ). (a) GbMNP-2; (b) GbMNP-3. Error bars represent the standard deviation of triplicate drug loading tests.

In general, it was observed that the drug loading capacity of GbMNPs increases with the increase of the initial DOX concentration. A maximum of 301  $\mu\text{g}\cdot\text{mg}^{-1}$  is obtained for GbMNP-2 when the DOX concentration in the solution is 250  $\mu\text{g}\cdot\text{mL}^{-1}$ , whereas GbMNP-3 reached 216  $\mu\text{g}\cdot\text{mg}^{-1}$  when the DOX concentration is 300  $\mu\text{g}\cdot\text{mL}^{-1}$ . The estimated loading contents of DOX in these cases were about 1.94  $\text{mg DOX m}^{-2}_{\text{GbMNP-2}}$  and 0.88  $\text{mg DOX m}^{-2}_{\text{GbMNP-3}}$ . It is interesting to observe that the sample with a higher hollow cavity and a larger specific surface area, GbMNP-3, presents a lower drug loading efficiency (DLE) and drug loading capacity profile. These unexpected results could be explained by the presence of a thicker graphene layer in the sample GbMNP-3, and the smaller pore sizes of this graphene-based shell (Figure 2c and Table 2). This combination could result in the fast clogging of the pores in the outer layers of the graphene shell with the drug molecules, restricting the access of the DOX molecules to the inner hollow cavity.

Nevertheless, these *in vitro* drug loading results show the remarkable capability of GbMNPs to load high contents of DOX. This ability can be attributed to the  $\pi$ - $\pi$  stacking and the possible presence of carboxylic acid groups, besides the epoxide and hydroxyl groups, on the graphene-based nanomaterials [41]. Seeking new insights on this phenomenon, the  $\text{pH}_{\text{PZC}}$ , i.e., the pH at which the surface charge is zero, was determined for the as-synthesized GbMNPs and functionalized GbMNPs. The  $\text{pH}_{\text{PZC}}$  of the as-synthesized GbMNPs is highly basic (pH  $\sim$ 12), possibly as an effect of the alkaline etching treatment to remove the silica template. On the other hand, the  $\text{pH}_{\text{PZC}}$  of the functionalized GbMNPs with  $\text{HNO}_3$  revealed strong acidic pH values ( $\sim$ 2.0), indicating that acidic groups, such as

carboxylic groups, were, in fact, formed during the chemical treatment. In addition, the  $pH_{PZC}$  of the functionalized GbMNPs allows us to conclude that their surface is negatively charged at the working pH for the drug delivery tests (pH  $\sim$ 6.0), i.e.,  $pH > pH_{PZC}$  [42]. On the other hand, at this working pH, the chemotherapeutic drug DOX is positively charged ( $pK_a \sim$ 8.3 [43]). These results indicate non-covalent interactions, such as electrostatic, between the nanocarriers (GbMNPs) and DOX.

### 3.3. In Vitro pH-Dependent Drug Release and Kinetics Studies

The exploration of pH differences between a tumour and a normal tissue's microenvironment motivates the development of smart nanocarriers designed as drug delivery systems able to be triggered by acidic pH values [23]. For this purpose, the cumulative pH-dependent DOX release profiles from the GbMNPs-DOX systems were assessed under different pH values, 7.4, 6.0, and 4.5, which mimics, respectively, the pH conditions found in healthy tissues, tumour microenvironment and intracellular tumour endosome/lysosome [23].

Graphene-based nanocarrier samples, GbMNP-2-DOX and GbMNP-3-DOX, show similar shape drug release profiles (Figure 6a,b, respectively).

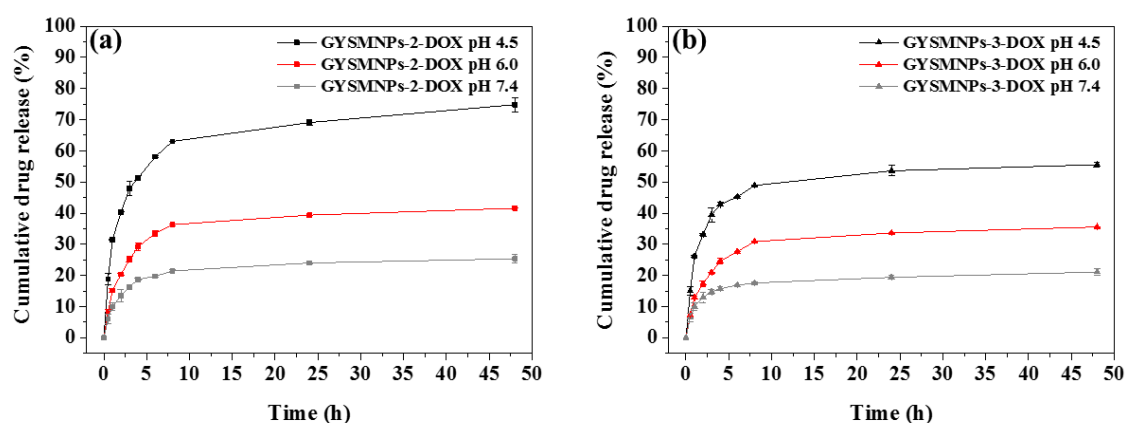


**Figure 6.** The pH-responsive release profiles of doxorubicin (DOX) from GbMNPs under different pH values (7.4, 6.0, and 4.5), at 37 °C. (a) GbMNP-2-DOX; (b) GbMNP-3-DOX. Error bars represent the standard deviation of triplicate drug release tests.

Analysis of the first incubation hour reveals that just a very low amount of DOX was released at physiological pH conditions (i.e., pH 7.4). At pH 6.0, the drug release was slightly higher than at pH 7.4, i.e., 15% versus 10% for GbMNP-2-DOX and 7% versus 6% for GbMNP-3-DOX, respectively. However, the nanocarriers reveal a remarkable increase of the released DOX (around 30% for sample GbMNP-2-DOX and 15% for sample GbMNP-3-DOX) at pH 4.5. For long-period drug release, only around 20% of DOX was released by both materials under physiological conditions after 48 h. Under pH 6.0, sample GbMNP-2-DOX released a maximum of 41% of DOX, whereas sample GbMNP-3-DOX released around 35% after the same period of time. Under intracellular acidic pH conditions, and after the initial burst release of up to 30%, sample GbMNP-2-DOX released a remarkable value of 75% of the encapsulated drug, and sample GbMNP-3-DOX, almost 56%. The outstanding pH-responsive drug release performance of GO is attributed to the presence of the  $\pi$ - $\pi$  stacking, as well as electrostatic interactions between the graphene-based nanostructures and aromatic DOX molecules [23]. Thus, in the presence of mild acidic environment such as the ones found in tumours, those interactions can be easily disrupted [14] by the increased solubility of DOX caused by the protonation process [18]. In this study, it was found that the pH-dependent controlled release phenomenon can be attributed to the loss of the negative surface of the nanocarriers' surface (GbMNPs), as the pH of the solutions goes from 7.4 to 4.5, and related to the charge increased protonation [23]. This increase of the surface charge causes a reduction of the electrostatic attraction between the GbMNPs and DOX protonated molecules, which leads to the increase of the drug release. Overall,

the in vitro pH-responsive drug release results suggest the great ability to use these nanocarriers as efficient drug encapsulation systems for local drug release.

The kinetic studies using the drug release data from GbMNPs are listed in Table 4. The Korsmeyer–Peppas model (with the higher  $R^2$  values) was considered the best one to describe the system. Moreover, the respective  $n$  values were below 0.45 in all cases, which means that the drug release is controlled by simple quasi-Fickian diffusion [23].

**Table 4.** The in vitro drug release kinetics studies of GbMNPs.

Sample	pH	Zero-Order	First-Order	Hixson-Crowell	Higuchi	Korsmeyer–Peppas	
		$R^2$	$R^2$	$R^2$	$R^2$	$R^2$	$n$
GbMNP-2	7.4	0.45	0.37	0.47	0.72	0.85	0.30
	6.0	0.46	0.35	0.50	0.73	0.84	0.33
	4.5	0.47	0.39	0.58	0.73	0.96	0.44
GbMNP-3	7.4	0.41	0.39	0.43	0.67	0.85	0.23
	6.0	0.48	0.37	0.51	0.74	0.85	0.33
	4.5	0.40	0.34	0.46	0.66	0.81	0.26

### 3.4. In Vitro Biocompatibility and Cellular Drug-Delivery Assay

Biocompatibility is a key feature for the potential application of nanomaterials in biological systems, where an ideal nanocarrier should ensure low or negligible toxicity. Biocompatibility of GbMNPs at different concentrations ( $0.12\text{--}30.0\ \mu\text{g}\cdot\text{mL}^{-1}$ ) was determined in PLP2 cells, and normalized to the cell viability in cell cultures for 48 h, at  $37\ ^\circ\text{C}$ .

The biocompatibility tests (Figure 7) reveal a very distinct behaviour between the developed nanocarriers, GbMNP-2 and GbMNP-3, tested in PLP2 cells. GbMNP-2, characterized by a few layer GO yolk-shell magnetic nanoparticles, exhibits good biocompatibility even at the high concentration of  $30.0\ \mu\text{g}\cdot\text{mL}^{-1}$ . On the other hand, GbMNP-3, characterized as a yolk-shell magnetic nanostructure coated with a defective multi-graphitic-layer shell, shows a severe cell inhibition behaviour at high concentrations of nanocarriers. Indeed, these results are in line with other results reported in the literature, where the cytotoxicity of different graphene-based nanomaterials has been discussed [44–46]. According to the available information, the lateral size, shape, number of layers, stiffness, hydrophobicity, surface functionalization, concentration dose, and chemistry of the graphene-based materials, all play an important role on the interaction of this type of material with cell membranes, intracellular uptake, and its cytotoxicity [46].

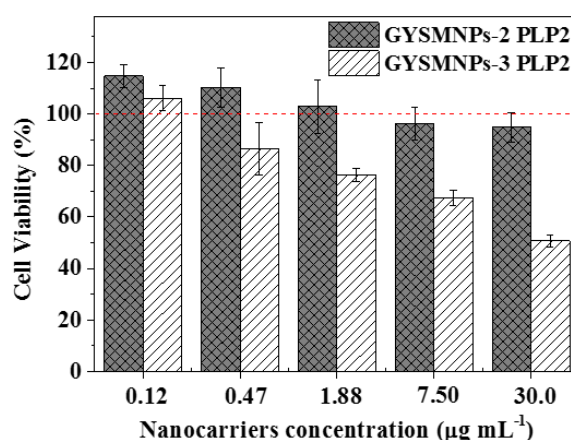


**Figure 7.** The in vitro biocompatibility study of GbMNPs in the primary cell culture (PLP2). Error bars represent a 95% confidence interval.

In addition, the in vitro cellular drug-delivery assays of free DOX and GbMNP-2 carrying DOX (GbMNP-2-DOX) were investigated in the tumour cell line, MCF-7, and compared with the primary cell culture cells, PLP2, as shown in Figure 8a,b.

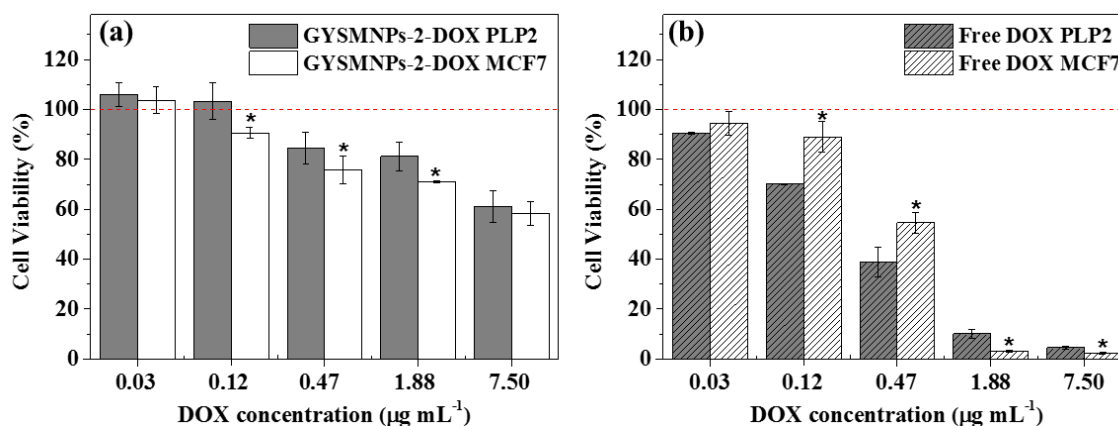


**Figure 8.** The in vitro cellular drug-delivery assays for several DOX concentrations, following 48 h of incubation. (a) GbMNP-2-DOX growth inhibition results tested in cancer cell line (MCF-7) and healthy cell line (PLP2); (b) free DOX growth inhibition results tested in the MCF-7 and PLP2 cell lines. Error bars represent a 95% confidence interval and the asterisks (\*) represent statistical significance in comparison with a healthy cell line, PLP2, for  $p < 0.05$  determined by the Student's  $t$ -test.

In both cell lines, MCF7 and PLP2, GbMNP-2-DOX nanocarriers and free DOX exhibit a dose-dependent cytotoxicity. It was also observed that free DOX shows more toxicity over the cell lines, especially over the healthy cell line PLP2 than in the DOX released from the nanocarriers at the time point investigated (48 h). Nevertheless, and in opposition with free DOX, the designed GbMNP-2 nanocarriers show the ability to preferentially deliver the chemotherapeutic drug into the cancer cells.

Therefore, the GbMNP-2 material exhibits remarkable combined characteristics for an efficient drug delivery, namely, a good loading capacity, high pH-sensitivity, high drug release at the mimic tumoral pH, high  $M_s$ , superparamagnetic behaviour, and biocompatibility.

#### 4. Conclusions

Graphene-based magnetic nanoparticles (GbMNPs) were developed for biomedical applications by using a simple tailor-made coating protocol. The results show the capability to synthesize GbMNPs with very distinctive physicochemical and toxicological properties, just by adjusting the number of carbon precursors. In particular, a hybrid magnetic nanomaterial was developed with exceptional characteristics (GbMNP-2) to be applied as a drug nanocarrier system. Impressively, this hybrid nanomaterial exhibited: (i) good colloidal stability in aqueous solutions; (ii) exceptional  $M_s$  value of  $69.8 \text{ emu} \cdot \text{g}^{-1}$ ; (iii) superparamagnetic behaviour; (iv) strong pH-triggered drug release response; and (v) biocompatibility. Additionally, the combination of these parameters also indicates a high potentiality to couple these magnetic nanocomposites with other biomedical applications, namely, magnetic hyperthermia and/or magnetic resonance imaging [47,48]. Therefore, the presented strategy reported in this work shows the potentiality to synthesize tailor-made graphene-based magnetic materials specially designed for the combined treatment of cancer.

**Author Contributions:** Conceptualization, R.O.R.; Data curation, G.D. and R.C.C.; Formal analysis, S.D. and J.G.; Funding acquisition, A.M.T.S.; Investigation, R.O.R.; Resources, G.B., M.B.-L., I.C.F.R.F. and H.T.G.; Supervision, G.B., R.L., A.M.T.S. and H.T.G.; Writing—original draft, R.O.R.; Writing—review & editing, J.G., M.B.-L., R.L., A.M.T.S. and H.T.G.

**Funding:** This research was funded by Project POCI-01-0145-FEDER-006984—Associate Laboratory LSRE-LCM funded by FEDER through COMPETE2020—Programa Operacional Competitividade e Internacionalização (POCI)—and by national funds through FCT—Fundação para a Ciência e a Tecnologia, and by project

NORTE-01-0145-FEDER-029394, RTChip4Theranostics, supported by Programa Operacional Regional do Norte—Norte Portugal Regional Operational Programme (NORTE 2020), under the PORTUGAL 2020 Partnership Agreement, through the European Regional Development Fund (ERDF) and by Fundação para a Ciência e Tecnologia (FCT), IP.

**Acknowledgments:** R.O.R. acknowledges the Ph.D. scholarship SFRH/BD/97658/2013 granted by FCT. G.D. acknowledges financing by Slovene Research Agency (J2-6754). The authors also would like to acknowledge the financial support provided by COST—European Cooperation in Science and Technology, in the form of a short term scientific mission (STSM) granted by COST Action TD1402: RADIOMAG.

**Conflicts of Interest:** The authors declare no conflict of interest.

## References

1. Li, Z.; Ye, E.; David; Lakshminarayanan, R.; Loh, X.J. Recent advances of using hybrid nanocarriers in remotely controlled therapeutic delivery. *Small* **2016**, *12*, 4782–4806. [[CrossRef](#)] [[PubMed](#)]
2. Mura, S.; Nicolas, J.; Couvreur, P. Stimuli-responsive nanocarriers for drug delivery. *Nat. Mater.* **2013**, *12*, 991–1003. [[CrossRef](#)] [[PubMed](#)]
3. Park, H.-Y.; Schadt, M.J.; Lim, I.I.S.; Njoki, P.N.; Kim, S.H.; Jang, M.-Y.; Luo, J.; Zhong, C.-J. Fabrication of Magnetic Core@Shell Fe Oxide@Au Nanoparticles for Interfacial Bioactivity and Bio-separation. *Langmuir* **2007**, *23*, 9050–9056. [[CrossRef](#)] [[PubMed](#)]
4. Robinson, I.; Tung, L.D.; Maenosono, S.; Wälti, C.; Thanh, N.T.K. Synthesis of core-shell gold coated magnetic nanoparticles and their interaction with thiolated DNA. *Nanoscale* **2010**, *2*, 2624–2630. [[CrossRef](#)] [[PubMed](#)]
5. Yang, Y.; Jiang, X.; Chao, J.; Song, C.; Liu, B.; Zhu, D.; Sun, Y.; Yang, B.; Zhang, Q.; Chen, Y.; et al. Synthesis of magnetic core-branched Au shell nanostructures and their application in cancer-related miRNA detection via SERS. *Sci. China Mater.* **2017**, *60*, 1129–1144. [[CrossRef](#)]
6. Jovanovic, A.V.; Flint, J.A.; Varshney, M.; Morey, T.E.; Dennis, D.M.; Duran, R.S. Surface Modification of Silica Core-Shell Nanocapsules: Biomedical Implications. *Biomacromolecules* **2006**, *7*, 945–949. [[CrossRef](#)] [[PubMed](#)]
7. Li, C.; Ma, C.; Wang, F.; Xil, Z.; Wang, Z.; Deng, Y.; Hel, N. Preparation and biomedical applications of core-shell silica/magnetic nanoparticle composites. *J. Nanosci. Nanotechnol.* **2012**, *12*, 2964–2972. [[CrossRef](#)] [[PubMed](#)]
8. Karimzadeh, I.; Aghazadeh, M.; Doroudi, T.; Ganjali, M.R.; Kolivand, P.H. Superparamagnetic Iron Oxide (Fe<sub>3</sub>O<sub>4</sub>) Nanoparticles Coated with PEG/PEI for Biomedical Applications: A Facile and Scalable Preparation Route Based on the Cathodic Electrochemical Deposition Method. *Adv. Phys. Chem.* **2017**, *2017*, 9437487. [[CrossRef](#)]
9. Medeiros, S.F.; Santos, A.M.; Fessi, H.; Elaissari, A. Stimuli-responsive magnetic particles for biomedical applications. *Int. J. Pharm.* **2011**, *403*, 139–161. [[CrossRef](#)] [[PubMed](#)]
10. Yallapu, M.M.; Foy, S.P.; Jain, T.K.; Labhassetwar, V. PEG-Functionalized Magnetic Nanoparticles for Drug Delivery and Magnetic Resonance Imaging Applications. *Pharm. Res.* **2010**, *27*, 2283–2295. [[CrossRef](#)] [[PubMed](#)]
11. Mody, V.V.; Cox, A.; Shah, S.; Singh, A.; Bevins, W.; Parihar, H. Magnetic nanoparticle drug delivery systems for targeting tumor. *Appl. Nanosci.* **2014**, *4*, 385–392. [[CrossRef](#)]
12. Tietze, R.; Zaloga, J.; Unterweger, H.; Lyer, S.; Friedrich, R.P.; Janko, C.; Pöttler, M.; Dürr, S.; Alexiou, C. Magnetic nanoparticle-based drug delivery for cancer therapy. *Biochem. Biophys. Res. Commun.* **2015**, *468*, 463–470. [[CrossRef](#)] [[PubMed](#)]
13. Huang, X.; Wu, S.; Du, X. Gated mesoporous carbon nanoparticles as drug delivery system for stimuli-responsive controlled release. *Carbon* **2016**, *101*, 135–142. [[CrossRef](#)]
14. Mohapatra, S.; Rout, S.R.; Das, R.K.; Nayak, S.; Ghosh, S.K. Highly Hydrophilic Luminescent Magnetic Mesoporous Carbon Nanospheres for Controlled Release of Anticancer Drug and Multimodal Imaging. *Langmuir* **2016**, *32*, 1611–1620. [[CrossRef](#)] [[PubMed](#)]
15. Zhang, Y.S.; Zhang, Y.N.; Zhang, W. Cancer-on-a-chip systems at the frontier of nanomedicine. *Drug Discov. Today* **2017**, *22*, 1392–1399. [[CrossRef](#)] [[PubMed](#)]
16. Jang, H.L.; Zhang, Y.S.; Khademhosseini, A. Boosting clinical translation of nanomedicine. *Nanomedicine* **2016**, *11*, 1495–1497. [[CrossRef](#)] [[PubMed](#)]

17. Hua, S.; de Matos, M.B.C.; Metselaar, J.M.; Storm, G. Current Trends and Challenges in the Clinical Translation of Nanoparticulate Nanomedicines: Pathways for Translational Development and Commercialization. *Front. Pharmacol.* **2018**, *9*, 790. [[CrossRef](#)] [[PubMed](#)]
18. Li, S.; Zheng, J.; Chen, D.; Wu, Y.; Zhang, W.; Zheng, F.; Cao, J.; Ma, H.; Liu, Y. Yolk-shell hybrid nanoparticles with magnetic and pH-sensitive properties for controlled anticancer drug delivery. *Nanoscale* **2013**, *5*, 11718–11724. [[CrossRef](#)] [[PubMed](#)]
19. Sasikala, A.R.K.; Thomas, R.G.; Unnithan, A.R.; Saravanakumar, B.; Jeong, Y.Y.; Park, C.H.; Kim, C.S. Multifunctional Nanocarpet for Cancer Theranostics: Remotely Controlled Graphene Nanoheaters for Thermo-Chemosensitisation and Magnetic Resonance Imaging. *Sci. Rep.* **2016**, *6*, 20543. [[CrossRef](#)] [[PubMed](#)]
20. Hummers, W.S.; Offeman, R.E. Preparation of Graphitic Oxide. *J. Am. Chem. Soc.* **1958**, *80*, 1339. [[CrossRef](#)]
21. Sarno, M.; Cirillo, C.; Scudieri, C.; Polichetti, M.; Ciambelli, P. Electrochemical Applications of Magnetic Core-Shell Graphene-Coated FeCo Nanoparticles. *Ind. Eng. Chem. Res.* **2016**, *55*, 3157–3166. [[CrossRef](#)]
22. Rodrigues, R.O.; Bañobre-López, M.; Gallo, J.; Tavares, P.B.; Silva, A.M.T.; Lima, R.; Gomes, H.T. Haemocompatibility of iron oxide nanoparticles synthesized for theranostic applications: A high-sensitivity microfluidic tool. *J. Nanopart. Res.* **2016**, *18*, 1–17. [[CrossRef](#)]
23. Rodrigues, R.O.; Baldi, G.; Doumett, S.; Garcia-Hevia, L.; Gallo, J.; Bañobre-López, M.; Dražić, G.; Calhelha, R.C.; Ferreira, I.C.F.R.; Lima, R.; et al. Multifunctional graphene-based magnetic nanocarriers for combined hyperthermia and dual stimuli-responsive drug delivery. *Mater. Sci. Eng. C* **2018**, *93*, 206–217. [[CrossRef](#)] [[PubMed](#)]
24. Liu, W.-J.; Liu, Y.-X.; Yan, X.-Y.; Yong, G.-P.; Xu, Y.-P.; Liu, S.-M. One-pot synthesis of yolk-shell mesoporous carbon spheres with high magnetisation. *J. Mater. Chem. A* **2014**, *2*, 9600–9606. [[CrossRef](#)]
25. Ribeiro, R.S.; Frontistis, Z.; Mantzavinos, D.; Venieri, D.; Antonopoulou, M.; Konstantinou, I.; Silva, A.M.T.; Faria, J.L.; Gomes, H.T. Magnetic carbon xerogels for the catalytic wet peroxide oxidation of sulfamethoxazole in environmentally relevant water matrices. *Appl. Catal. B Environ.* **2016**, *199*, 170–186. [[CrossRef](#)]
26. Abreu, R.M.V.; Ferreira, I.C.F.R.; Calhelha, R.C.; Lima, R.T.; Vasconcelos, M.H.; Adegas, F.; Chaves, R.; Queiroz, M.-J.R.P. Anti-hepatocellular carcinoma activity using human HepG2 cells and hepatotoxicity of 6-substituted methyl 3-aminothieno[3,2-b]pyridine-2-carboxylate derivatives: In vitro evaluation, cell cycle analysis and QSAR studies. *Eur. J. Med. Chem.* **2011**, *46*, 5800–5806. [[CrossRef](#)] [[PubMed](#)]
27. Svobodova, B.; Barros, L.; Calhelha, R.C.; Heleno, S.; Alves, M.J.; Walcott, S.; Bittova, M.; Kuban, V.; Ferreira, I.C.F.R. Bioactive properties and phenolic profile of *Momordica charantia* L. medicinal plant growing wild in Trinidad and Tobago. *Ind. Crops Prod.* **2017**, *95*, 365–373. [[CrossRef](#)]
28. Bharath, G.; Madhu, R.; Chen, S.-M.; Veeramani, V.; Mangalaraj, D.; Ponpandian, N. Solvent-free mechanochemical synthesis of graphene oxide and Fe<sub>3</sub>O<sub>4</sub>-reduced graphene oxide nanocomposites for sensitive detection of nitrite. *J. Mater. Chem. A* **2015**, *3*, 15529–15539. [[CrossRef](#)]
29. Feng, Y.; Feng, N.; Wei, Y.; Zhang, G. An in situ gelatin-assisted hydrothermal synthesis of ZnO-reduced graphene oxide composites with enhanced photocatalytic performance under ultraviolet and visible light. *RSC Adv.* **2014**, *4*, 7933–7943. [[CrossRef](#)]
30. Wang, N.; Yang, Z.; Xu, F.; Thummavichai, K.; Chen, H.; Xia, Y.; Zhu, Y. A generic method to synthesise graphitic carbon coated nanoparticles in large scale and their derivative polymer nanocomposites. *Sci. Rep.* **2017**, *7*, 11829. [[CrossRef](#)] [[PubMed](#)]
31. Lim, J.; Ryu, S.Y.; Kim, J.; Jun, Y. A study of TiO<sub>2</sub>/carbon black composition as counter electrode materials for dye-sensitized solar cells. *Nanoscale Res. Lett.* **2013**, *8*, 227. [[CrossRef](#)] [[PubMed](#)]
32. Ribeiro, R.S.; Silva, A.M.T.; Tavares, P.B.; Figueiredo, J.L.; Faria, J.L.; Gomes, H.T. Hybrid magnetic graphitic nanocomposites for catalytic wet peroxide oxidation applications. *Catal. Today* **2017**, *280*, 184–191. [[CrossRef](#)]
33. Xu, Z.; Chen, Y.; Li, W.; Li, J.; Yu, H.; Liu, L.; Wu, G.; Yang, T.; Luo, L. Preparation of boron nitride nanosheet-coated carbon fibres and their enhanced antioxidant and microwave-absorbing properties. *RSC Adv.* **2018**, *8*, 17944–17949. [[CrossRef](#)]
34. Ferrari, A.C.; Meyer, J.C.; Scardaci, V.; Casiraghi, C.; Lazzeri, M.; Mauri, F.; Piscanec, S.; Jiang, D.; Novoselov, K.S.; Roth, S.; et al. Raman Spectrum of Graphene and Graphene Layers. *Phys. Rev. Lett.* **2006**, *97*, 187401. [[CrossRef](#)] [[PubMed](#)]
35. Ferrari, A.C.; Robertson, J. Interpretation of Raman spectra of disordered and amorphous carbon. *Phys. Rev. B* **2000**, *61*, 14095–14107. [[CrossRef](#)]

36. Bianco, A.; Cheng, H.-M.; Enoki, T.; Gogotsi, Y.; Hurt, R.H.; Koratkar, N.; Kyotani, T.; Monthieux, M.; Park, C.R.; Tascon, J.M.D.; et al. All in the graphene family—A recommended nomenclature for two-dimensional carbon materials. *Carbon* **2013**, *65*, 1–6. [[CrossRef](#)]
37. Kaniyoor, A.; Ramaprabhu, S. A Raman spectroscopic investigation of graphite oxide derived graphene. *AIP Adv.* **2012**, *2*, 032183. [[CrossRef](#)]
38. Mohan, P.; Rapoport, N. Doxorubicin as a Molecular Nanotheranostic Agent: Effect of Doxorubicin Encapsulation in Micelles or Nanoemulsions on the Ultrasound-Mediated Intracellular Delivery and Nuclear Trafficking. *Mol. Pharm.* **2010**, *7*, 1959–1973. [[CrossRef](#)] [[PubMed](#)]
39. Mahdavi, M.; Rahmani, F.; Nouranian, S. Molecular simulation of pH-dependent diffusion, loading, and release of doxorubicin in graphene and graphene oxide drug delivery systems. *J. Mater. Chem. B* **2016**, *4*, 7441–7451. [[CrossRef](#)]
40. Al-Nahain, A.; Lee, S.Y.; In, I.; Lee, K.D.; Park, S.Y. Triggered pH/redox responsive release of doxorubicin from prepared highly stable graphene with thiol grafted Pluronic. *Int. J. Pharm.* **2013**, *450*, 208–217. [[CrossRef](#)] [[PubMed](#)]
41. Pastrana-Martínez, L.M.; Morales-Torres, S.; Likodimos, V.; Falaras, P.; Figueiredo, J.L.; Faria, J.L.; Silva, A.M.T. Role of oxygen functionalities on the synthesis of photocatalytically active graphene-TiO<sub>2</sub> composites. *Appl. Catal. B Environ.* **2014**, *158–159*, 329–340. [[CrossRef](#)]
42. Al-Degs, Y.S.; El-Barghouthi, M.I.; El-Sheikh, A.H.; Walker, G.M. Effect of solution pH, ionic strength, and temperature on adsorption behavior of reactive dyes on activated carbon. *Dyes Pigments* **2008**, *77*, 16–23. [[CrossRef](#)]
43. Adnan, A.; Lam, R.; Chen, H.; Lee, J.; Schaffer, D.J.; Barnard, A.S.; Schatz, G.C.; Ho, D.; Liu, W.K. Atomistic Simulation and Measurement of pH Dependent Cancer Therapeutic Interactions with Nanodiamond Carrier. *Mol. Pharm.* **2011**, *8*, 368–374. [[CrossRef](#)] [[PubMed](#)]
44. Chen, D.; Dougherty, C.A.; Zhu, K.; Hong, H. Theranostic applications of carbon nanomaterials in cancer: Focus on imaging and cargo delivery. *J. Control. Release* **2015**, *210*, 230–245. [[CrossRef](#)] [[PubMed](#)]
45. Sanchez, V.C.; Jachak, A.; Hurt, R.H.; Kane, A.B. Biological Interactions of Graphene-Family Nanomaterials—An Interdisciplinary Review. *Chem. Res. Toxicol.* **2012**, *25*, 15–34. [[CrossRef](#)] [[PubMed](#)]
46. Zhang, B.; Wang, Y.; Zhai, G. Biomedical applications of the graphene-based materials. *Mater. Sci. Eng. C* **2016**, *61*, 953–964. [[CrossRef](#)] [[PubMed](#)]
47. Kumeria, T.; Maher, S.; Wang, Y.; Kaur, G.; Wang, L.; Erkelens, M.; Forward, P.; Lambert, M.F.; Evdokiou, A.; Losic, D. Naturally Derived Iron Oxide Nanowires from Bacteria for Magnetically Triggered Drug Release and Cancer Hyperthermia in 2D and 3D Culture Environments: Bacteria Biofilm to Potent Cancer Therapeutic. *Biomacromolecules* **2016**, *17*, 2726–2736. [[CrossRef](#)] [[PubMed](#)]
48. Ma, X.; Tao, H.; Yang, K.; Feng, L.; Cheng, L.; Shi, X.; Li, Y.; Guo, L.; Liu, Z. A functionalized graphene oxide-iron oxide nanocomposite for magnetically targeted drug delivery, photothermal therapy, and magnetic resonance imaging. *Nano Res.* **2012**, *5*, 199–212. [[CrossRef](#)]

